nature communications

Article

https://doi.org/10.1038/s41467-025-68266-3

Increased electromagnetic interference shielding and load bearing with a three-dimensional pristine graphene@pyrocarbon skeleton in AZ91D

Received: 27 December 2024

Accepted: 23 December 2025

Published online: 15 January 2026

Check for updates

Yuan Ma[1], Lingjun Guo[1], Yuchen Cao[1] & Lehua Qi[2]

The development of electronic devices for communication systems, radar warning, and satellite detection requires lightweight materials that exhibit exceptional electromagnetic interference (EMI) shielding while maintaining mechanical robustness. However, designing three-dimensional (3D) structured pristine graphene (PG) that achieves both high EMI shielding and substantial load-bearing capacity remains a significant challenge. In this work, an innovative method of 3D skeleton preconstruction-infiltration filling is proposed. This approach demonstrates that molten AZ91D is infiltrated into the 3D structured PG@pyrocarbon (PG@PyC), and its 3D structure can be maintained in the AZ91D matrix via a liquid-solid infiltration extrusion method. By utilizing this strategy, PG@PyC reinforced AZ91D matrix (PG@PyC/AZ91D) composites display remarkable comprehensive performance, realizing an EMI shielding effectiveness of 76.70 dB (at 3 mm thickness), ultimate compressive strength of 276 MPa, and ultimate tensile strength of 231 MPa. The developed composites are promising lightweight materials for the integration of structural and functional applications in complex environments.

With the rapid advancement of next-generation electronic communication systems, radar warning, satellite detection, and deep space exploration play a crucial role in the fields of aerospace, information technology, and daily life[1–5]. To guarantee the normal operation of these systems, it is both a goal and a challenge to develop electronic device casings that integrate outstanding electromagnetic interference (EMI) shielding performance with mechanical stability and lightweight characteristics[6–8].

Nowadays, three-dimensional (3D) structured graphene has shown excellent EMI shielding properties by virtue of good conductivity and porous microstructures[9–11]. There are still significant obstacles for it to bear loads as a rigid structural material. This issue restricts the application of 3D structured graphene in electronic device casings that require both excellent EMI shielding performance and robust load-bearing capability. It is an innovative strategy to introduce a high-stiffness component (molten Mg alloy) into the pores of 3D structured graphene, thereby enabling the Mg alloy to act as a rigid load-bearing component. By leveraging the advantages of continuous connectivity inherent in the 3D network structure of graphene embedded within the Mg alloy matrix, efficient electron and load transfer can be achieved. The construction of 3D structured graphene within the Mg alloy and the design of heterointerfaces are key factors affecting the performance of the composites.

There are many processing routes, including liquid-state fabrication methods (casting[12], selective laser melting[13], etc.) and solid-state fabrication techniques (powder metallurgy[14], friction stir processing[15], etc.) for the preparation of graphene reinforced Mg matrix (G/Mg) composites to solve the problem of graphene aggregation[16–19].

[1]Shaanxi Key Laboratory of Fiber Reinforced Light Composite Materials, Northwestern Polytechnical University, Xi'an, China. [2]School of Mechanical Engineering, Northwestern Polytechnical University, Xi'an, China. e-mail: qilehua@nwpu.edu.cn

Graphene can uniformly disperse at grain boundaries and impede grain growth of Mg, thereby enhancing the strength-ductility compatibility of G/Mg composites via the above methods. Nevertheless, the current preparation methods of G/Mg composites mentioned above are insufficient for constructing 3D network-structured graphene within the Mg matrix. An innovative strategy of 3D skeleton preconstruction-infiltration filling based on a liquid-solid infiltration extrusion method presents an intriguing solution. This approach first constructs a 3D graphene skeleton, which is subsequently infiltrated with molten Mg alloy, effectively maintaining the 3D network structure of the graphene. The liquid-solid infiltration extrusion method, including low-pressure infiltration followed by high-pressure densification, was independently developed by our research group[20].

The preservation of the 3D structure of graphene, along with the design of heterogeneous interfaces between graphene and Mg alloy, is crucial for optimizing the overall properties of the composites. On one hand, among many derivatives of graphene, pristine graphene (PG) exhibits fewer defects and a lower content of oxygen-containing functional groups, allowing it to fully leverage its intrinsic properties (lightweight, high conductivity, large specific surface area, and superior mechanical performance)[7,21,22]. However, constructing a 3D network-structured PG preform with substantial compressive strength poses a challenge due to its weak gelation ability[23]. On the other hand, the design and construction of heterogeneous interfaces between PG and Mg are of great significance for multi-component composites to achieve excellent EMI shielding and enhanced mechanical performance[24]. However, the poor interface of PG/Mg composites would be detrimental to the attenuation of electromagnetic waves (EMWs) within the composites and load transfer efficiency. It is crucial to introduce gradient interface layers to improve both the compressive strength of the PG preform and the interface bonding of the composites.

Herein, we present an innovative synthesis of PG@pyrocarbon (PG@PyC) reinforced AZ91D matrix (PG@PyC/AZ91D) composites, achieved through the preconstruction of a 3D PG@PyC skeleton followed by molten AZ91D infiltration filling. The prepared composites show exceptional EMI shielding performance and mechanical properties. Our design leverages the construction of a 3D connected PG@PyC network within the AZ91D matrix through this method, which can not only provide multiple reflections and scatterings of the EMWs and enhance interfacial polarization but also achieve a better load transfer strengthening effect. This innovative concept paves a way to obtain excellent lightweight structural-functional materials and shows promise for applications in next-generation electronic communication systems.

Results

Morphologies and structures of PG@PyC preforms

The synthesis process of preforms and composites is shown in Supplementary Fig. 1. The initial step in the proposed strategy (3D skeleton preconstruction-infiltration filling) is to fabricate a multifunctional 3D PG@PyC preform that exhibits both EMI shielding and mechanical performance. Methane (CH_4) was introduced as a carbon source at 1070–1080 °C for 60, 90, and 120 min on the PG preform, and the obtained preforms were named PG@PyC-60, PG@PyC-90, and PG@PyC-120, respectively. When the deposition time of PyC is 60–120 min, PyC would significantly affect the compressive strength and porosity of the PG@PyC preform, thereby affecting the overall properties of the composite. Figure 1 and Supplementary Fig. 2 show the morphologies of the PG and PG@PyC preforms, where PG sheets interconnect to generate a 3D network. In Fig. 1a1-d4, the 3D honeycomb structure can be retained even after deposition, and the uniform pore diameter is 15–80 μm. The PG sheets are uniformly coated with PyC, consisting of granular particles (0.2–1.5 μm). As the deposition time increases, the granular PyC gradually grows. The deposition of PyC would thicken the PG sheets (Fig. 1e1, f1, g1, h1, i1, i2, j1, and j2). PyC is grown on the PG sheets with an interlayer spacing of ~0.34 nm (Fig. 1e2, f2, g2, and h2). The selected area electron diffraction (SAED) pattern of PG changes from a hexagonal structure to a circular ring composed of symmetrical diffraction patterns on both sides after depositing PyC, indicating that the crystallinity of PyC is inferior to that of PG. There are more and more continuous carbon layers arranged on the PG sheets with the increase in deposition time.

The entire process of precursor pyrolysis and PyC deposition is analyzed through elementary reactions and morphologies of the PG@PyC preform, as shown in Fig. 2 and Supplementary Table 1. The rate constants are fitted according to the modified Arrhenius expression[25] (Supplementary Equation (1)). The precursor pyrolysis of PyC progresses from CH_4 to C_2-species, followed by C_4-species and C_6-species. To elucidate the reactions that play significant roles in the conversion of CH_4 to C_6H_6, the reaction enthalpy (ΔH) and Gibbs free energy change (ΔG) of each elementary reaction are calculated by HSC software, and the results are shown in Fig. 2a–f. Notable differences in ΔH and ΔG values are observed across different reactions. Reactions with higher rates and lower ΔG values are likely to be predominant during the precursor pyrolysis process. The first aromatic ring (C_6H_6) would be condensed to polycyclic aromatic hydrocarbons (PAHs). In the initial stage of deposition, C_2H_2 and C_2H_4 primarily react at the edge carbon atoms of PG, supplemented by the nucleation of PAHs on the PG or newly formed aromatic carbon planes. Figure 2g-j show the morphologies of the PG@PyC preforms when the deposition time of PyC is 20 min and 40 min, respectively. Some small granular PyC is grown on the PG sheets. A cross-linked structure between PyC and PG can be formed (Fig. 2j). As the deposition time increases, granular PyC is deposited and gradually merges until the PG substrate is completely covered, which can be further confirmed by Fig. 1b4, c4, and d4. The above schematic diagram of the PyC deposition process is displayed in Fig. 2k.

XRD, Raman spectroscopy, and XPS are employed to investigate the structure evolution of PG and PG@PyC. A primary peak located at 25.5-26.5° is identified as the (002) plane of graphite in Fig. 3a. Moreover, the interlayer spacing (d_{002}), mean microcrystalline height (L_c(002)), and graphitization degree (g) are calculated by Supplementary Equations (2)-(4)[26] and the results are listed in Supplementary Table 2. It is evident that with increasing deposition time, an increase in d_{002} and a decrease in both L_c(002) and g for PG@PyC preforms are obtained. The PG@PyC-60 preform exhibits a lower graphitization degree, a more disordered carbon layer structure, and a smaller graphene microcrystalline size than the PG preform. The defects in carbon materials can be detected by Raman spectroscopy, and the results are given in Fig. 3b and c. There are three typical vibration peaks (D, G, and 2D bands) in PG preform, while the PG@PyC preforms show two obvious characteristic peaks (D and G bands). The Raman spectra of PG@PyC are fitted with five Lorenz curves located at 1200 cm^{-1} (D_4), 1350 cm^{-1} (D), 1500 cm^{-1} (D_3), 1580 cm^{-1} (G), and 1620 cm^{-1} (D′)[27]. After depositing PyC, highly defective D_3 and D_4 bands appear, while the 2D band of the graphene lattice disappears, indicating a significant difference in graphitization degree between PG and PyC. The G band reflects the graphitic degree related to the in-plane motion of sp^2 carbon atoms in the carbon materials[4,28]. Since the graphitization degree of PyC is lower than that of the PG, the G peak of PG@PyC would decrease sharply after depositing PyC on the PG in Fig. 3b. The width of graphene microcrystals (L_a) can be calculated from the intensity ratio of D band to G band (I_D/I_G, Supplementary Equation (5)[29]), as shown in Supplementary Table 3. The I_D/I_G value increases from 0.15 to 1.13 after depositing PyC, accompanied by a decrease in L_a from 29.33 nm to 3.89 nm. The chemical compositions of PG@PyC preforms are elucidated through XPS spectra in Fig. 3d, e. The high-resolution C 1s spectrum is deconvoluted into four sub-peaks at 284.5 eV, 285.5 eV, 286.5 eV, and 289.0 eV, which correspond to C-C (sp^2), defect peak (sp^3), C-O, and O-C = O bonds, respectively. The area

https://doi.org/10.1038/s41467-025-68266-3

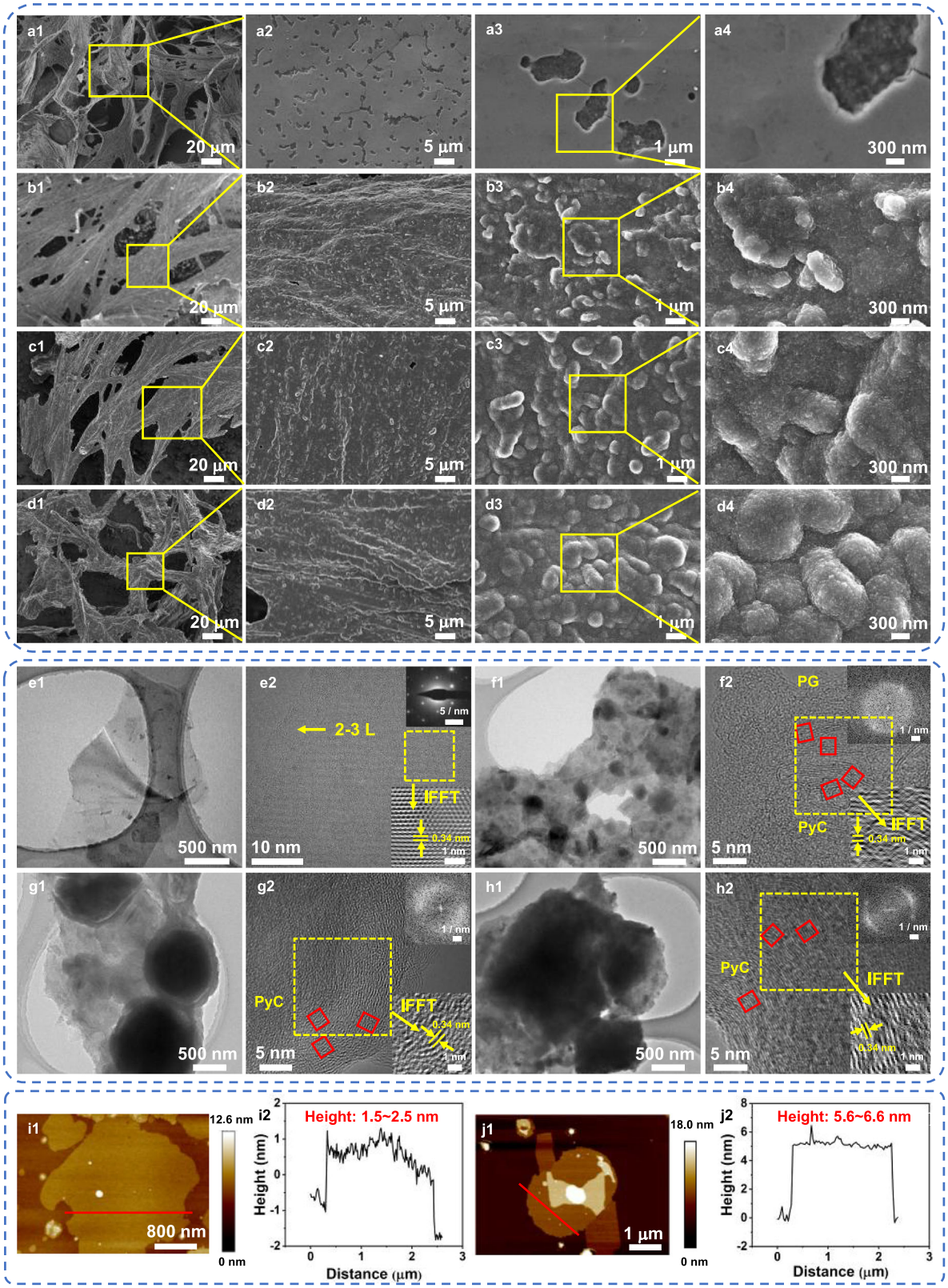

Fig. 1 | SEM, TEM, and AFM images of preforms. a1–**a4** SEM images of PG preform. **b1**–**b4** SEM images of PG@PyC-60 preform. **c1**–**c4** SEM images of PG@PyC-90 preform. **d1**–**d4** SEM images of PG@PyC-120 preform. **e1**, **e2** TEM images of PG sheets. **f1**, **f2** TEM images of PG@PyC-60 sheets. **g1**, **g2** TEM images of PG@PyC-90 sheets. **h1**, **h2** TEM images of PG@PyC-120 sheets. **i1**, **i2** AFM images of PG sheets. **j1**, **j2** AFM images of PG@PyC-60 sheets. The AFM image height (nm) is shown by the color bar. Pristine graphene and pyrocarbon are defined as PG and PyC, respectively. Inverse fast fourier transform is abbreviated as IFFT.

https://doi.org/10.1038/s41467-025-68266-3

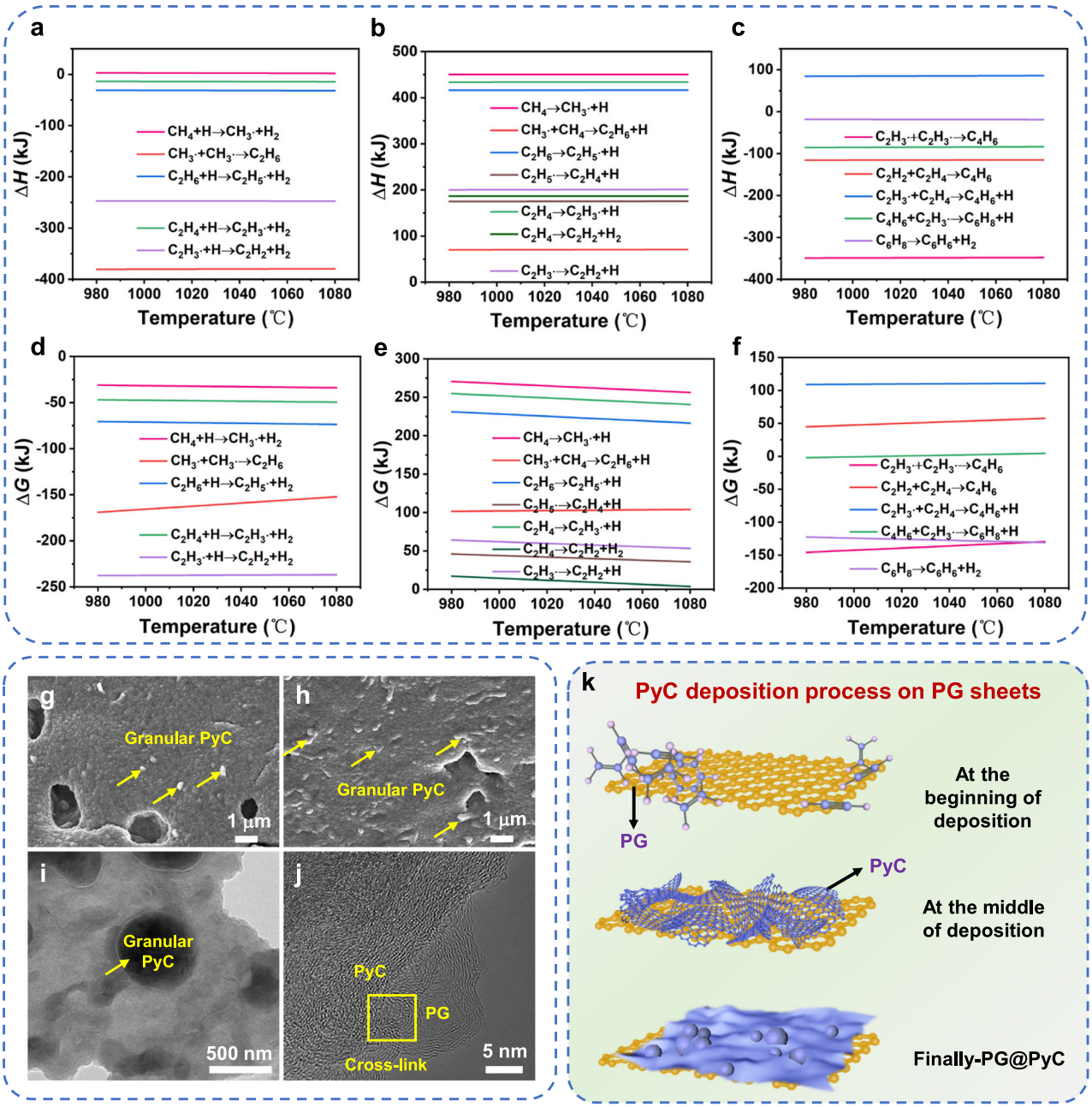

Fig. 2 | The entire process of precursor pyrolysis and PyC deposition. **a**–**c** Reaction enthalpy (*H*) and **d**–**f** Gibbs free energy change (*G*) of each elementary reaction among the reactions from CH_4 to C_6H_6 calculated by HSC software. **g** SEM image of PG@PyC-20 preform. **h**–**j** SEM and TEM images of PG@PyC-40 preform. Pristine graphene and pyrocarbon are defined as PG and PyC, respectively. **k** Schematic diagram of the PyC deposition process.

ratio of sp^3 to sp^2 (sp^3/sp^2) serves as an indicator of the defect level within carbon materials. Notably, the sp^3/sp^2 ratio of PG@PyC preforms shows an increase with higher PyC content. It demonstrates that the introduction of PyC leads to an increase in defects and structural disorder inside the materials, which can enhance dipole polarization loss and attenuation of EMWs[28].

The surface roughness of the preforms and the contact angles between molten AZ91D droplets and preforms are displayed in Fig. 3f. The roughness parameters *Sa* and *Sq* are calculated by Supplementary Equations (6)-(7)[30,31]. Compared with PG preform, the *Sa* values of PG@PyC-60, PG@PyC-90, and PG@PyC-120 are 31.2 μm, 44.1 μm, and 51.9 μm, respectively, showing increases of 100.00%, 182.69%, and 232.69%. The wetting angle test is detailed in the Supplementary Methods. The contact angles between AZ91D droplet and PG, PG@PyC-60, PG@PyC-90, and PG@PyC-120 preforms are 111°, 123°, 131°, and 128°, respectively. An extended deposition time of PyC leads to an increase in both surface roughness and contact angle. Although the interface between PyC and AZ91D is in a non-wetting state, the enhanced surface roughness of PG endowed by PyC would form a tight interlocking effect with the matrix, making it difficult for PG and Mg to slide along the interface and strengthening the interfacial bonds[32,33]. The compressive stress-strain curves of PG, PG@PyC, and pure PyC preforms are shown in Fig. 3g, h. The preparation process of pure PyC preform is detailed in the Supplementary Methods. The compressive strengths of PG, PyC-60, PyC-90, and PyC-120 preforms are 4 kPa, 34 kPa, 66 kPa, and 113 kPa under 50.0% deformation, respectively. In contrast, the compressive strengths of PG@PyC-60, PG@PyC-90, and PG@PyC-120 preforms are 35 kPa, 69 kPa, and 120 kPa, significantly

https://doi.org/10.1038/s41467-025-68266-3

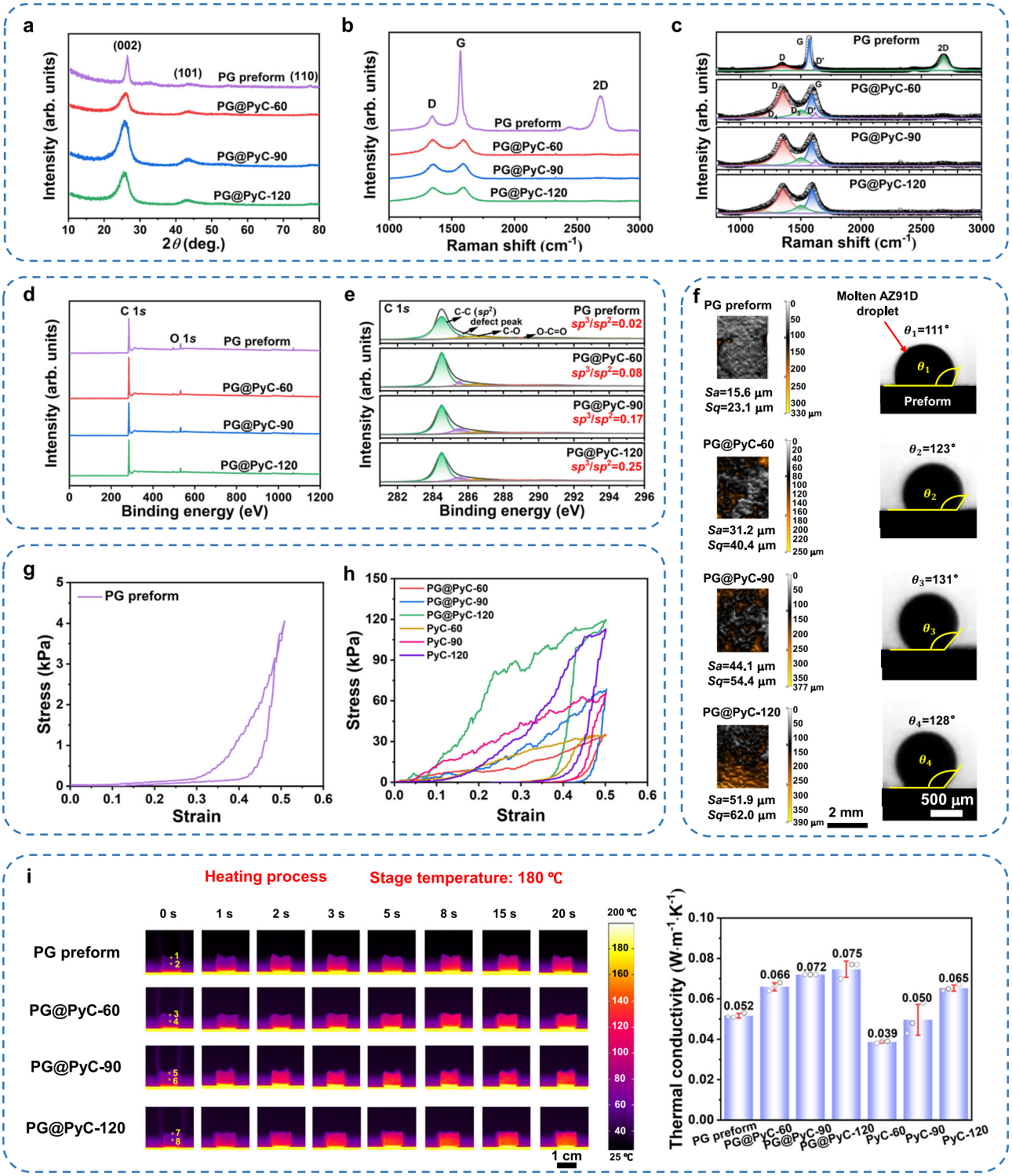

Fig. 3 | Characterization of PG, PG@PyC, and pure PyC preforms. a XRD patterns. **b**, **c** Raman spectra. **d** Wide-scan XPS spectra. **e** High-resolution XPS of C 1*s*. **f** Surface roughness of preform and contact angles between molten AZ91D droplet and preform. The height of the surface (μm) is shown by the color bar. **g**, **h** Compressive stress-strain curves. **i** Infrared images and thermal conductivity. The temperature (°C) is shown by the color bar. Data are presented as mean values ± standard deviations (SD) from $n = 3$ impendent experiments.

increasing by 8.75, 17.25, and 30.00 times, respectively, compared with the PG preform. The deposition of PyC increases the thickness of the cell walls of the PG preform, significantly improving its compressive strength. The PG@PyC preforms demonstrate remarkable mechanical stability, which is essential for withstanding the infiltration pressure of the molten AZ91D during the preparation of the composites.

The thermal management capability of preforms can be estimated by the infrared thermal imaging method and measurements of thermal conductivity (Fig. 3i and Supplementary Fig. 3). The thermal conductivities of the PyC-60, PyC-90, and PyC-120 preforms are 0.039 $W•m^{-1}•K^{-1}$, 0.050 $W•m^{-1}•K^{-1}$, and 0.065 $W•m^{-1}•K^{-1}$, respectively. The thermal conductivities of PG preform increase from 0.052 $W•m^{-1}•K^{-1}$ to

0.066 $W•m^{-1}•K^{-1}$, 0.072 $W•m^{-1}•K^{-1}$, and 0.075 $W•m^{-1}•K^{-1}$, respectively, after depositing different contents of PyC. The thermal conductivity of both pure PyC and PG@PyC preforms rises with increasing PyC content. The PG and PG@PyC preforms are placed on a hot stage at 180 °C, and then an infrared thermal camera is used to record the temperature during heating. It is found that the heating rates of all PG@PyC preforms exceed that of the PG preform. Thermal conduction in the 3D structured PG preform comprises solid heat conduction, gas heat conduction, and radiative heat conduction[34]. An increase in carbon content coupled with a reduction in porosity within the preform enhances solid heat conduction, thereby improving thermal conductivity.

The EMI shielding performance, calculated by Supplementary Equations (8)–(14), is related to the electrical conductivity (Supplementary Fig. 4) of the preform, which plays a crucial role in that of the composites. The EMI shielding effectiveness (SE) of the preforms in the X band is presented in Fig. 4a and b. The PG preform exhibits a low EMI SE value of 25.62 dB, whereas the EMI SE values of PG@PyC increase significantly to 35.28 dB, 80.50 dB, and 77.77 dB, respectively, with rising PyC content. The enhancement in EMI SE_T with more PyC content aligns with the corresponding increase in electrical conductivity of the preform. In Fig. 4c, the reflection coefficient (*R*) gradually improves with extended growth time, surpassing the absorption coefficient (*A*), demonstrating that the primary shielding mechanism of the PG@PyC preform is the reflection process.

The EMI shielding mechanism is illustrated in Fig. 4d. When incident EMWs reach the surface of the PG@PyC preform, most are shielded due to the impedance mismatch between the preform and free space. Electrically conductive networks with numerous charge carriers enhance EMI SE through reflection. The remaining EMWs penetrate into the preform and are dissipated by the following processes. Firstly, PG shows a high G peak while PyC exhibits a low G peak due to their different graphitization degrees, resulting in abundant heterogeneous interfaces. The mismatch of electrical conductivity between PG and PyC results in significant interfacial polarization. When subjected to an alternating EM field, variations in charge carrier mobility and polarization response rates across different dielectric materials cause free charges to accumulate at the PG-PyC interface. The network structure with many interfaces and conductivity mismatches would enhance charge storage capacity and amplify interfacial polarization[35]. Secondly, the 3D network structure of the PG@PyC preform provides pathways for electron motion and EMWs transmission through multiple reflections and scatterings. With the increase of PyC content, more cross-linking among PG sheets and more electron transfer pathways can be obtained. Thirdly, Raman analysis indicates that PyC contains various lattice defects, inducing dipole polarization under an alternating EM field[36]. Consequently, the EMI SE increases with the PyC content. Compared with PG@PyC-90, the EMI shielding performance of PG@PyC-120 is reduced. This reduction can be attributed to the fact that the increased deposition of PyC tends to cover some small pores within the preform. Consequently, this leads to a diminished capacity for electron and phonon transport within the 3D structure. In summary, these findings demonstrate a multifunctional PG@PyC-90 preform, which achieves excellent EMI shielding performance, thermal transfer efficiency, and mechanical stability.

Microstructures of composites

Through the liquid-solid infiltration extrusion method, the obtained composites were designated as PG/AZ91D, PG@PyC-60/AZ91D, PG@PyC-90/AZ91D, and PG@PyC-120/AZ91D composites, respectively, corresponding to different preforms. Based on the extrusion direction during the preparation of the composites (Supplementary Fig. 5), the composites both perpendicular and parallel to the extrusion direction are selected for SEM characterization. The infiltration temperature of molten AZ91D (Supplementary Fig. 6), the concentration of PG (Supplementary Fig. 7), and the introduction of PyC significantly influence the microstructures of the composites. Fig. 5a1–d4 illustrates the microstructures of the composites with varying PyC content grafted at their interfaces. In these composites, the black areas pointed by yellow arrows represent PG and PG@PyC, while lighter areas correspond to the Mg matrix. For both PG/AZ91D and PG@PyC-60/AZ91D composites, aggregated PG sheets (marked with red boxes), small pores within those sheets, and the disrupted network can be observed in Fig. 5a1–b4. As indicated in Fig. 5a3, a4, b3, and b4, it is evident that the distribution of PG sheets tends to align perpendicularly to the extrusion direction, which proves that the preforms undergo flattening during the infiltration process, resulting in the agglomeration of PG. It can be attributed to the lower compressive strength of both PG and PG@PyC-60 preforms, which are unable to withstand the infiltration pressure. In contrast, when the growth time of PyC is prolonged to 90 min, the arrangement of PG becomes more homogenous, and the continuous 3D network of PG@PyC remained intact in the composites (Fig. 5c1-c3), verified by 3D reconstruction results (Fig. 5e and Supplementary Movies 1-3). The PG@PyC-90 preform with enhanced compressive strength can resist the infiltration pressure, which helps to maintain the uniform network structure of PG@PyC in the AZ91D matrix and prevent re-agglomeration. Additionally, some small pores in the PG layers are also well infiltrated in Fig. 5c4. Regarding the PG@PyC-120/AZ91D composites (Fig. 5d1–d4), it is found that a lamellar structure with partially interconnected bridges of PG@PyC is dispersed in the AZ91D matrix. A pressure exceeding 30 kPa is needed to overcome capillary infiltration resistance and achieve complete pore filling according to the Washburn equation[37] (Supplementary Equation (15)). This requires the preform to have adequate compressive strength. During the infiltration process, molten AZ91D is flown into the PG@PyC preform under an external pressure of 30-40 kPa, without damaging the 3D structure of PG@PyC-90 and PG@PyC-120 preforms. The molten AZ91D moves from the top to the bottom and from the edges to the core regions within the preform[38]. This infiltration process remains stable, with pores gradually being filled by molten AZ91D. When the infiltration temperature is appropriate (~660 °C) and the compressive strength of the preform is sufficiently high (more than 40 kPa), uniform and adequate infiltration of molten AZ91D can be achieved without any non-infiltration regions. To decrease or eliminate possible existing pores, various strategies drawn on the techniques associated with the squeeze casting process or vacuum casting process can be employed, including controlling extrusion temperature[39], applying high pressure during solidification[40], lowering cavity air pressure[41], combining vacuum with the casting process[42], and so on.

There are white particle precipitations near the PG in the composites, marked as Spot A-C and confirmed by EDS in Fig. 5f and Supplementary Table 4. The white particle precipitations contain Al and Mn elements with an atomic ratio close to 8:5. Fig. 5g shows the XRD patterns of AZ91D and composites, revealing that AZ91D and all composites display typical diffraction peaks of α-Mg. The primary constituents of AZ91D are α-Mg and $Mg_{17}Al_{12}$ phases[43]. The $Mg_{17}Al_{12}$ phase can be characterized in the PG@PyC/AZ91D composites. However, the $Mg_{17}Al_{12}$ phase is not detected in the PG/AZ91D composites due to its low content. The presence of $Mg_{17}Al_{12}$ phase in the PG/AZ91D composites can be proven by the TEM images (Supplementary Fig. 8). The peaks of Al_8Mn_5 appear in the PG/AZ91D and PG@PyC/AZ91D composites. Mn is almost insoluble in α-Mg and would react with Al solute to form Al_8Mn_5 rather than forming intermetallic compounds (IMCs) with Mg[44]. Al_8Mn_5 can be formed at various stages during handling, solidification, and heat treatment of AZ91D melt[45–47], leading to a reduction in the content of the $Mg_{17}Al_{12}$ phase. The diffraction peak of PG is only detected in the PG/AZ91D composites due to the abundance of PG clusters. No aluminum carbides are found in the

https://doi.org/10.1038/s41467-025-68266-3

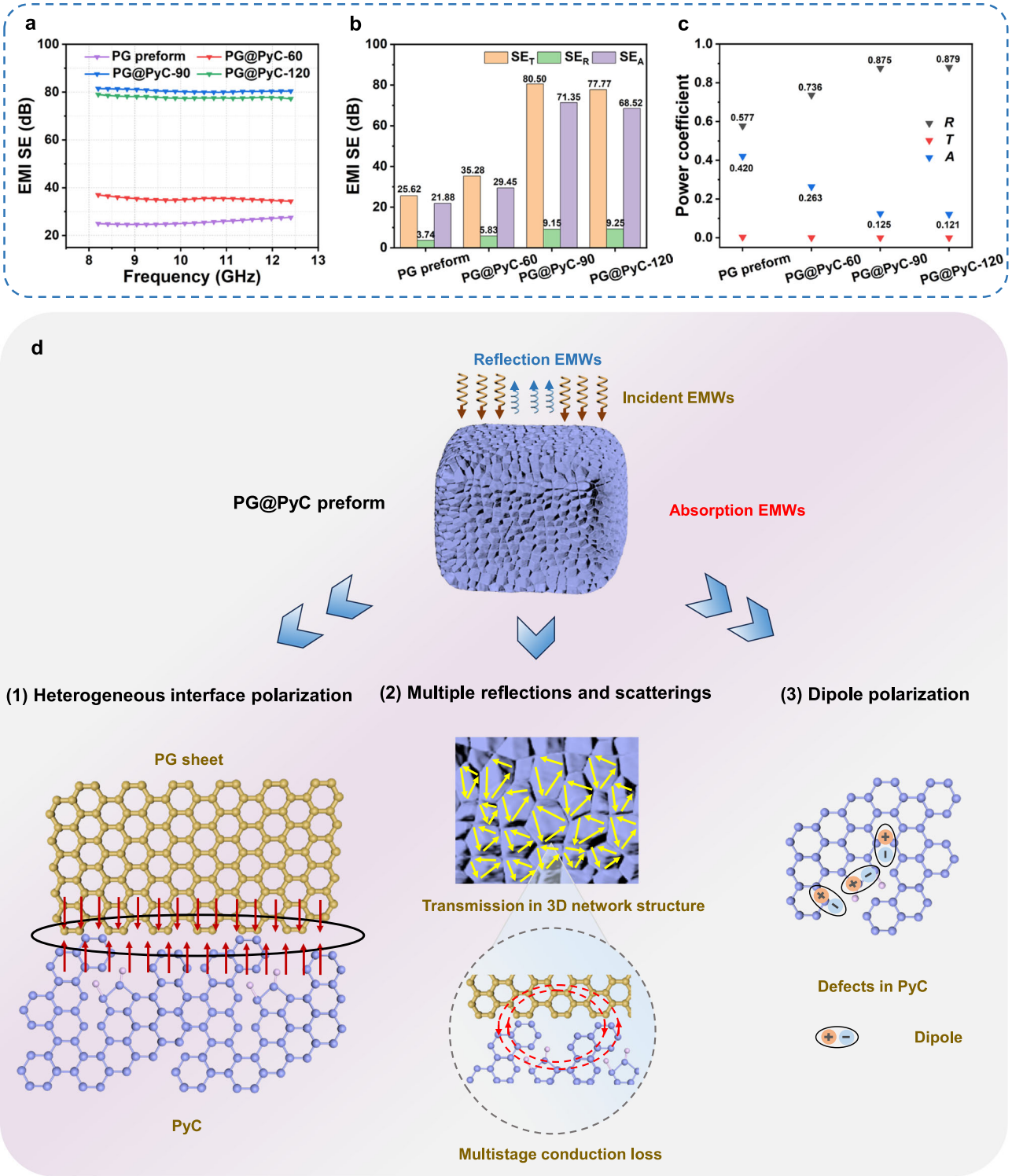

Fig. 4 | EMI shielding performance. a, **b** EMI SE values in the X band. **c** Average *R*, *T*, and *A* values. Reflection coefficient (*R*), transmission coefficient (*T*), and absorption coefficient (*A*) represent the ability of reflection, transmission, and absorption of the EMWs, respectively. **d** Schematic diagram of the EMI shielding mechanism of PG@PyC preform. When incident EMWs reach the surface of the PG@PyC preform, most are shielded. The remaining absorption EMWs are dissipated by heterogeneous interface polarization loss, multiple reflections and scatterings, multistage conduction loss, and dipole polarization loss.

composites, as highly purified carbon materials (PG and PyC) would not react with Al, even at relatively high temperatures[48]. Figure 5h and Supplementary Fig. 9 present the Raman spectra of the composites. The increase in the I_D/I_G value of the PG/AZ91D is greater than that of the other composites after the preparation of the composites. This means that even though the preparation process of the composites may induce structural damage to the PG, PyC would protect PG and effectively enhance its performance.

Interfacial structures of composites

The interfacial structures between PG and AZ91D matrix are crucial in determining the EMI shielding and mechanical properties of the

https://doi.org/10.1038/s41467-025-68266-3

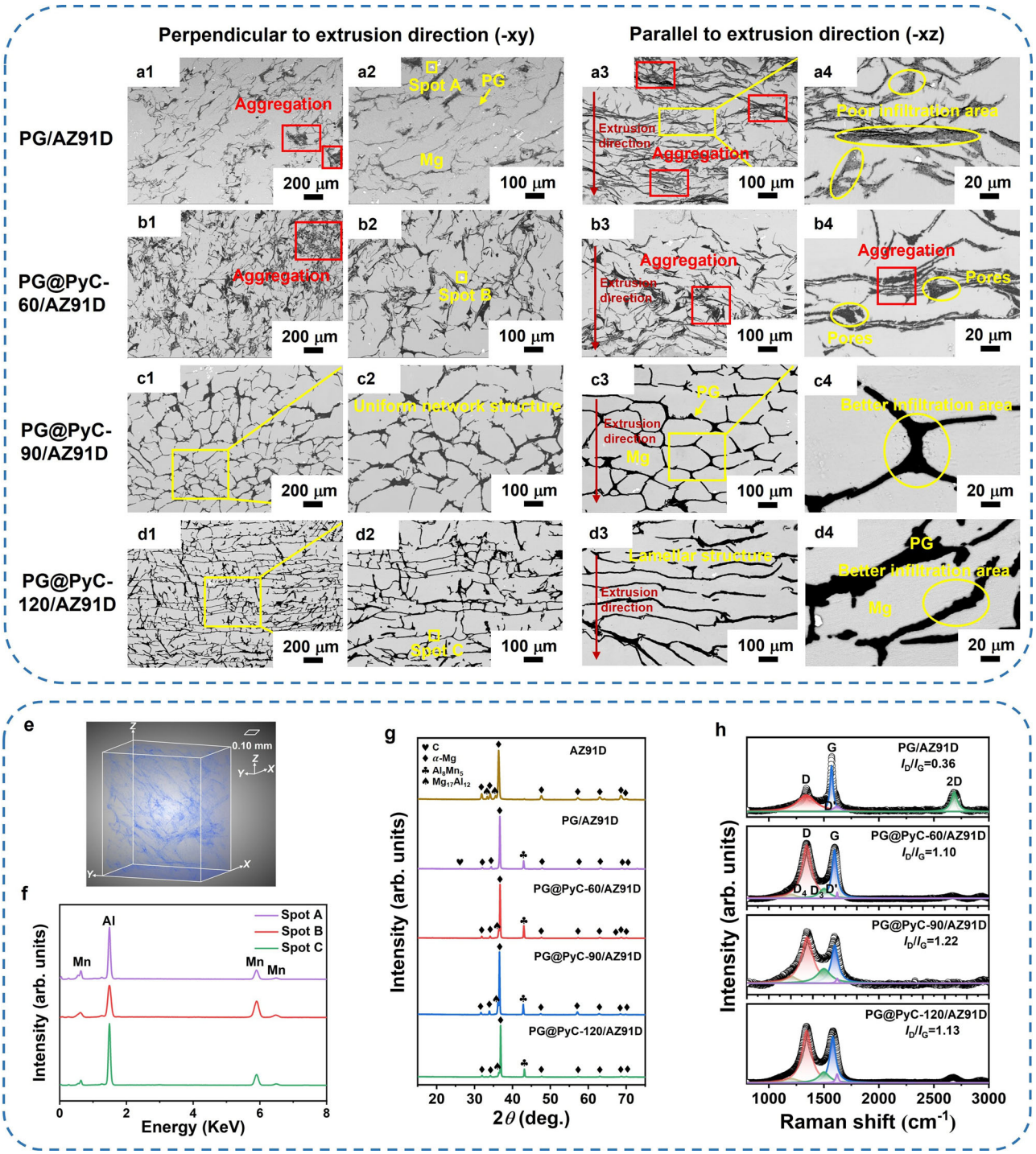

Fig. 5 | Characterization of the composites. a1–a4 SEM images of PG/AZ91D composites. **b1–b4** SEM images of PG@PyC-60/AZ91D composites. **c1–c4** SEM images of PG@PyC-90/AZ91D composites. **d1–d4** SEM images of PG@PyC-120/AZ91D composites. The composites both perpendicular (*x*-*y* plane) and parallel (*x*-*z* plane) to the extrusion direction are selected for SEM characterization. **e** 3D reconstruction result of 3D PG@PyC in the PG@PyC-90/AZ91D composites. The composites were characterized using an X-ray microscope (ZEISS, Xradia 515 Versa), resulting in a series of 2D section images. The 3D reconstruction result can be obtained from this collection of 2D images through image segmentation, surface reconstruction, and visualization utilizing Dragonfly 2021 software. **f** EDS spectra of Spot A-C in (a2), (b2), and (d2), respectively. **g** XRD diffractions of AZ91D and composites. **h** Raman spectra of the composites.

composites. TEM images of the composites are shown in Fig. 6. There are no interfacial products in the PG/AZ91D composites (Fig. 6a1 and a2), displaying mechanical bonding between PG and Mg. A disordered area and mutual diffusion (PG-Mg) are evident at the interface in Fig. 6a3 (yellow boxes). Furthermore, some dislocations are presented near the interface. HRTEM image of Area C (Fig. 6a4) reveals that PG comprises multiple layers of graphene. After introducing PyC, PyC-MgO rich zones are tightly embedded within the PG and matrix in Fig. 6b1–b3, c1, c2, c5, d1-d3, and d5. As the deposition time of PyC is prolonged, the thickness of the PyC-MgO transition layer increases, with the values of ~8.6 nm (PG@PyC-60/AZ91D), ~18.4 nm (PG@PyC-90/AZ91D), and ~314.5 nm (PG@PyC-120/AZ91D), respectively. From Fig. 6b3, c2, c5, and d5, dispersed nanoparticles (marked with yellow circles) accompanied by PyC at the interface can be confirmed as MgO

https://doi.org/10.1038/s41467-025-68266-3

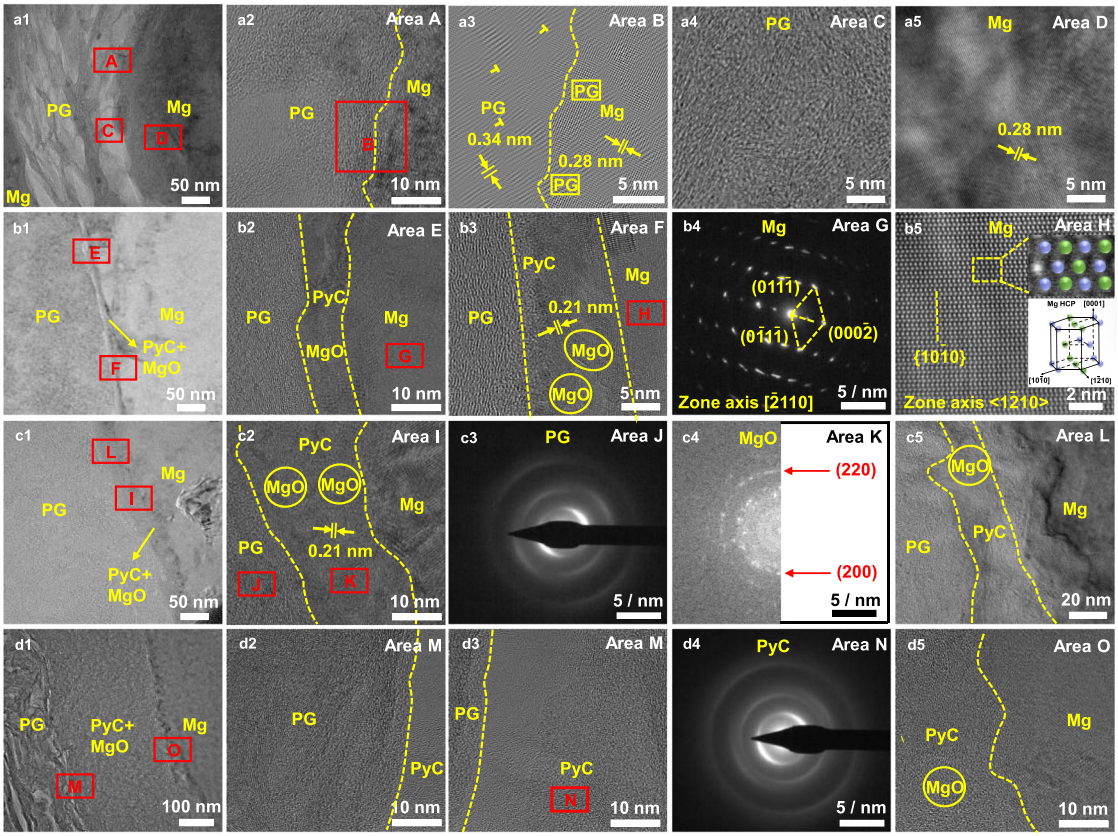

Fig. 6 | Interface structures of a1-a5 PG/AZ91D, b1-b5 PG@PyC-60/AZ91D, c1-c5 PG@PyC-90/AZ91D, and d1-d5 PG@PyC-120/AZ91D composites. a1, **b1**, **c1**, **d1** TEM images. **a2** HRTEM image of Area A in (a1). **a3** IFFT image of Area B in (a2). **a4** HRTEM image of Area C in (a1). **a5** HRTEM image of Area D in (a1). **b2** HRTEM image of Area E in (b1). **b3** HRTEM image of Area F in (b1). **b4** SAED pattern of Area G in (b2). **b5** Atomic-resolution HAADF-STEM image of Area H in (b3) (inset image: schematic diagram of HCP Mg). **c2** HRTEM image of Area I in (c1). **c3** SAED pattern of Area J in (c2). **c4** FFT pattern of Area K in (c2). **c5** HRTEM image of Area L in (c1). **d2**, **d3** HRTEM images of Area M in (d1). **d4** SAED pattern of Area N in (d3). **d5** HRTEM image of Area O in (d1). Pristine graphene and pyrocarbon are defined as PG and PyC, respectively.

phase, which exhibits an interlayer spacing of 0.21 nm and polycrystalline rings (Fig. 6c4). The MgO nanoparticles are formed in situ by the reaction between molten Mg and oxygen-containing groups on the PyC, as supported by ΔH and ΔG (Supplementary Equation (16) and Supplementary Fig. 10). The molten Mg would not react with C from either PG or PyC, which can be confirmed by Supplementary Fig. 11. It can be attributed to the following reasons. There is no wetting between C and Mg, which makes it challenging for the two elements to engage in chemical reactions. Moreover, magnesium carbides such as MgC_2 and Mg_2C_3 are thermodynamically unstable. When the temperature is below 450 °C and 670 °C, they will decompose, respectively[49,50]. Unlike magnesium carbides, MgO is a thermodynamically stable phase[49,50]. Therefore, MgO can be obtained stably while the magnesium carbides cannot be formed. After depositing PyC on PG, PG@PyC comprises multiple disordered carbon layers (Fig. 6b3, c2, d2, and d3). The SAED patterns of PG and PyC are both circular rings (Fig. 6c3 and d4) due to the diffusion of PyC onto the PG. Mg can be determined by the HRTEM images (an inter-planar spacing of 0.28 nm in Fig. 6a5) and SAED pattern (Fig. 6b4). It discloses that the Mg (01$\bar{1}$1) plane is along the Mg [$\bar{2}$110] zone axis. Fig. 6b5 shows an atomic-resolution HAADF-STEM image of Mg, with an inset displaying a repeatable stacking unit of the Mg lattice along <1$\bar{2}$10>. It indicates that Mg has a hexagonal close-packed (hcp) structure with an ABAB stacking arrangement. The PG is well-bonded to Mg through the PyC-MgO transition layer. The lattice distortion of the PG/PyC-MgO/Mg heterogeneous interface would induce more lattice defects and sufficient carriers to strengthen interfacial polarization and consume EMWs. The in-situ grown PyC, accompanied by MgO nanoparticles, would improve interfacial bonding and enhance load transfer efficiency[51].

EMI shielding and mechanical performances of composites

Figure 7a, b and Supplementary Fig. 12 show the EMI shielding performance of the AZ91D and composites in the X band. All samples were prepared with a thickness of 3 mm for EMI shielding evaluation, with the exception of the PG@PyC-90/AZ91D composite, which was also assessed at 2 mm. After introducing PG, the average SE_T value of the PG/AZ91D composites increases from 21.81 dB to 26.13 dB. As the deposition time of PyC is extended to 60 min, 90 min, and 120 min, the corresponding SE_T values are 36.71 dB, 76.70 dB, and 57.54 dB, respectively. The average SE_T value of the PG@PyC-90/AZ91D composites with a thickness of 2 mm is 69.59 dB. When the thickness of the material is much greater than the skin depth, increasing the thickness of the material has little effect on the EMI shielding performance[52]. The skin depth, which is related to electrical conductivity (Supplementary Fig. 13), can be calculated by Supplementary Equations (17)–(18)[53], as shown in Supplementary Fig. 14. Compared with AZ91D, the enhancement in SE_T values of the composites can be attributed to the improved SE_A values with no obvious variation in SE_R values. The SE_R of the composites can also be expressed as Supplementary Equation (14)[54]. The minimal change in SE_R is attributed to slight variations in electrical conductivity. The designed 3D network structure of PG@PyC in the AZ91D matrix promotes higher SE_A compared to that of the lamellar structure, resulting in an increased SE_T value of PG@PyC-90/AZ91D in contrast to the PG@PyC-120/AZ91D composites. In Fig. 7a, a

https://doi.org/10.1038/s41467-025-68266-3

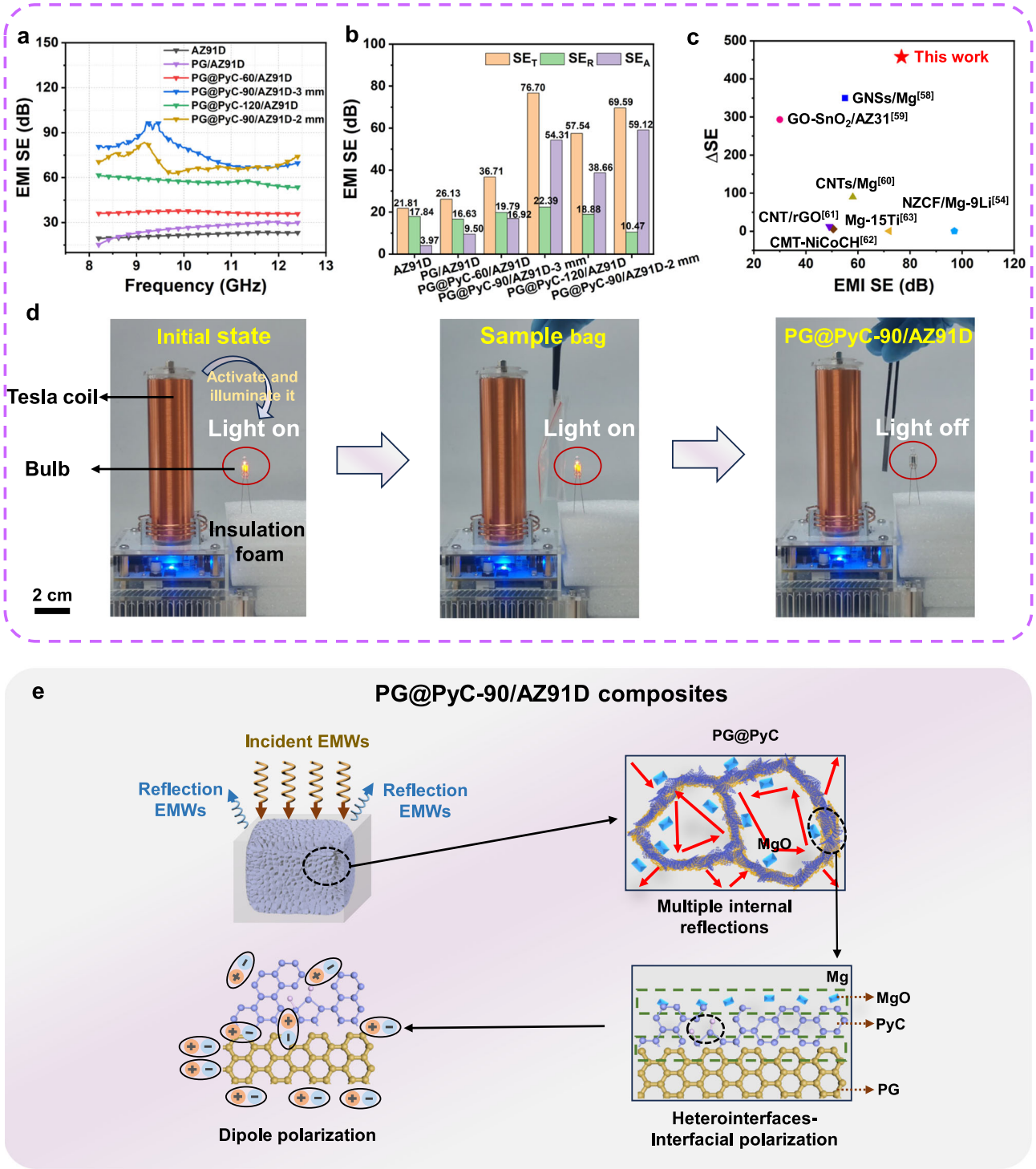

Fig. 7 | EMI shielding properties of AZ91D and composites. a, **b** EMI SE values. **c** Comparison of EMI shielding performance (SE values with various EMI SE values (X band)) between existing studies and this work. **d** Verification test of PG@PyC-90/AZ91D composite as an EMI shielding material. **e** Schematic diagram of the EMI shielding mechanism of PG@PyC-90/AZ91D composites. The EMWs are reflected at the surface of the composites when they reach the surface of the composites. The absorption attenuation within the composites can mainly come from conductive loss, multiple internal reflections, interfacial polarization, and dipole polarization.

peak between 9.2 GHz and 9.5 GHz is found in the PG@PyC-90/AZ91D composites, while the peak has not been found in AZ91D and other composites. It suggests the presence of resonance behavior[55] in the PG@PyC-90/AZ91D composites. The special 3D network structure of PG@PyC-90 in the AZ91D matrix induces eddy current effects and resonances that contribute to dielectric loss, resulting in high-performance EMI shielding and resonance behavior[56]. Existing studies indicate that the EMI SE values reaching near 100 dB in Mg alloy or Mg matrix composites are mainly based on the Mg-Li system with the unique α-Mg/β-Li dual-phase[54,57]. The EMI SE value of Mg-Li matrix composites increases from 77-96 dB to 89-100 dB due to the introduction of reinforcements (MWCNT or $Ni_{0.4}Zn_{0.4}Co_{0.2}Fe_2O_4$), representing an improvement of 4-30%[54,57]. To highlight the enhancement effect of PG@PyC in this work, comparisons of shielding performance (enhancement efficiency (ΔSE) of the materials with various EMI SE values) of the PG@PyC-90/AZ91D composites with other graphene-

based, Mg matrix composites, and Mg alloys are shown in Fig. 7c and Supplementary Table 5[54,58–63]. The ΔSE value can be evaluated by Supplementary Equation (19)[58]. A significant ΔSE value of 457.6 can be obtained, which is much higher than other existing studies. The remarkable strengthening efficiency and EMI SE value highlight the distinct advantage of constructing 3D network-structured PG@PyC within the AZ91D matrix.

To validate the EMI shielding performance of the PG@PyC-90/AZ91D composites, we employed a Tesla coil wireless power transmission system as the EM emission source[53]. As indicated in Fig. 7d and Supplementary Movie 4, when the PG@PyC-90/AZ91D composite is placed between the Tesla coil and bulb, the light is immediately off, demonstrating that the EMW signal can be effectively shielded by the PG@PyC-90/AZ91D composite. The primary factors for the enhancement of the EMI shielding property of the PG@PyC-90/AZ91D composites are summarized in Fig. 7e. Firstly, EMWs are reflected at the surface of the composites due to impedance mismatch. Secondly, the rest of the EMWs enter into the composites. The absorption attenuation within the composites can mainly come from dielectric loss and multi-level reflections. Dielectric loss is related to the dielectric conductivity and dielectric polarization[54]. On one hand, the highly connected 3D-PG@PyC establishes extensive conductive pathways and provides conductive loss. On the other hand, the PG/PyC-MgO/Mg heterointerfaces would generate more lattice defects, which in turn increase carrier density. This enhancement promotes an uneven distribution and accumulation of spatial charges at the heterojunction contact, thereby promoting interfacial polarization and facilitating the absorption of EMWs[59]. The numerous heterointerfaces, dislocations, grain boundaries, and phase boundaries further contribute to the interfacial polarization. Moreover, defects and oxygen-containing functional groups on PyC are conducive to the dipole polarization, which results in energy consumption.

The nano-indentation technique can be used to evaluate the enhancement effects of PG and PyC. The suffixes -xy and -xz refer to the application of a 5 mN load on the *x-y* and *x-z* planes of the composites, respectively. As shown in Fig. 8a–d, the introduction of PG leads to a reduction in penetration depth compared to the AZ91D, demonstrating the strengthening effect of PG on the AZ91D matrix. As the deposition time of PyC increases, the indentation depth initially becomes shallower, then deeper, followed by shallower again. This trend is also observed in both hardness and elastic modulus. In comparison with AZ91D, the PG@PyC-90/AZ91D composites are endowed with increments of 34.00% in hardness (1.34 GPa) and enhancements of 5.82% and 4.96% in elastic modulus (49.30 GPa and 48.90 GPa), respectively. The mechanical properties are further investigated through compressive and tensile strength experiments (Fig. 8e–h, Supplementary Fig. 15, Supplementary Fig. 16, Supplementary Fig. 17, and Supplementary Fig. 18). The ultimate compressive strength (UCS) and failure strain of AZ91D (remolten AZ91D by liquid-solid infiltration extrusion method) are 247 MPa and 15.6%, respectively. Due to the agglomeration of PG in the AZ91D matrix, the UCS values of the PG/AZ91D and PG@PyC-60/AZ91D composites are lower than that of AZ91D, making it unable to exert the strengthening effect of PG. The UCS and failure strain of the PG@PyC-90/AZ91D composites are enhanced gradually and exhibit the best values of 276 MPa and 21.0%, getting 58.62% and 40.00% improvements, respectively, compared with PG/AZ91D composites. Compared to AZ91D, the ultimate tensile strengths (UTS) of the composites firstly decrease to 98 MPa and

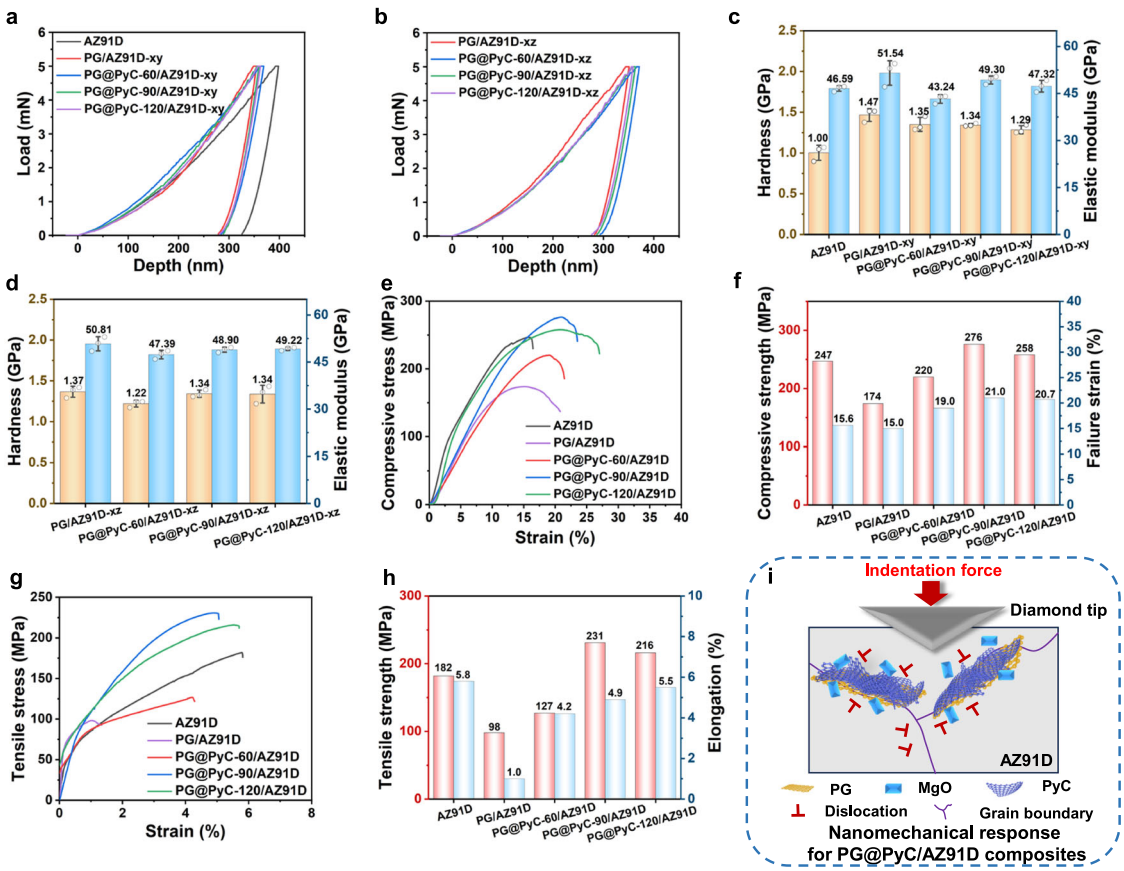

Fig. 8 | Mechanical performances of AZ91D and composites. a, **b** Nano-indentation curves. **c**, **d** Histogram of hardness and elastic modulus. Data are presented as mean values ± SD from $n = 3$ impendent experiments. **e** Compressive stress-strain curves. **f** Histogram of UCS and failure strain. **g** Tensile stress-strain curves. **h** Histogram of UTS and elongation. **i** Schematic diagram of the nano-mechanical response for PG@PyC/AZ91D composites.

127 MPa, and then increase to 231 MPa and 216 MPa with the addition of PG and PyC. The UTS is increased by 26.92% for PG@PyC-90/AZ91D composites and by 18.68% for PG@PyC-120/AZ91D composites, respectively, in contrast to AZ91D. The elongation of the PG@PyC-90/AZ91D composites is 4.9%. It indicates that constructing 3D network-structured PG@PyC in the AZ91D matrix contributes to simultaneously enhancing the UCS and UTS of the composites. The strengthening mechanism can be explained by the grain size of α-Mg in the composites, as presented in Supplementary Fig. 19, Supplementary Fig. 20, and Fig. 8i. The PG is distributed along the grain boundaries of α-Mg, which serves to restrict the growth of α-Mg grains and limit the migration of grain boundaries[64,65]. The PG/PyC-MgO/Mg interfaces facilitate load transfer. Both dislocation and fine grain size significantly enhance the reinforcing effect of PG, thereby facilitating superior nanomechanical strengthening.

Discussion

This work presents an innovative method of 3D skeleton preconstruction-infiltration filling. A continuous 3D PG@PyC network in the AZ91D matrix is fabricated using the liquid-solid infiltration extrusion method, aimed at producing lightweight structural-functional materials that achieve excellent EMI shielding performance and mechanical stability. Benefiting from the special conductive interconnected structure of the 3D PG@PyC in the AZ91D matrix, an EMI SE value of 76.70 dB for the PG@PyC-90/AZ91D composites can be obtained. The PG@PyC-90/AZ91D composite exhibits optimal mechanical properties, including a UCS of 276 MPa, UTS of 231 MPa, elastic modulus of 49.30 GPa, and hardness of 1.34 GPa. The approach of constructing a 3D multifunctional PG@PyC network within the AZ91D matrix has been proven to improve EMI shielding and mechanical properties. Structural-functional Mg matrix composites hold significant potential for applications across various fields, including the aerospace industry, information technology, and daily life.

Methods

Materials

PG sheets were synthesized from the liquid phase exfoliation method. AZ91D alloy (Mg-8.41 wt.% Al-0.65 wt.% Zn-0.22 wt.% Mn-0.05 wt.% Si-0.0025 wt.% Ni) was purchased from Dongguan Gelan Metal Materials Co., Ltd. All gases were sourced from Xi'an Weiguang Gas Co., Ltd. Poly(vinyl alcohol) (PVA, alcoholysis: 72.5-74.5 mol.%, viscosity: 4.2-5.0 mPa•s), riboflavin sodium phosphate (RP, USP), and sodium dodecyl sulfate (SDS, GR) were bought from Shanghai Aladdin Biochemical Technology Co., Ltd. and Shanghai Macklin Biochemical Co., Ltd., respectively. All reagents were used without further purification.

Fabrication of PG and PG@PyC preforms

PG preform was prepared by self-assembly combined with freeze-drying methods. PG sheets (10.0 mg•mL^{-1}, 50 mg), PVA (2.0 mg•mL^{-1}, 10 mg), RP (0.4 mg•mL^{-1}, 2 mg), and SDS (15.0 mg•mL^{-1}, 75 mg) were first mixed in aqueous solution using bath ultrasound and then stirred for 5 min at 300 rpm and 3 min at 1200 rpm. Then, the mixture was frozen at −20 °C for 24-72 h and dried to obtain the PG preform. Finally, the PG preform was heat-treated at 900 °C for 90 min, protected by Ar. The PG@PyC preforms were prepared by depositing PyC onto the PG sheets in a chemical vapor deposition furnace using a mixture of CH_4 and Ar.

Preparation of PG/AZ91D and PG@PyC/AZ91D composites

AZ91D was heated to 600–700 °C, then infiltrated into the PG preform and PG@PyC preforms via the liquid-solid infiltration extrusion method. The liquid-solid infiltration extrusion method includes low-pressure infiltration followed by high-pressure densification. A low pressure of 30-40 kPa was applied to facilitate the infiltration of molten AZ91D into the pores of the 3D structured PG@PyC preform, ensuring that the 3D structure remained intact during processing at elevated temperatures. Subsequently, a high pressure of 20–60 MPa was applied to the AZ91D in its liquid-solid state (520–560 °C) to realize densification of the composites without compromising the integrity of the 3D skeleton of the PG@PyC.

Characterization

Field emission scanning electron microscope (SEM, Zeiss Sigma 300) with energy-dispersive spectroscopy (EDS) and double Cs corrector transmission electron microscope (TEM, FEI, Themis Z) were used to investigate the morphologies of the PG preform, PG@PyC preforms, and composites. Optical microscope (OM, Nikon ECLIPSE LV150N) was applied to observe the microstructures of the AZ91D and composites. Atomic force microscope (AFM, Bruker, Dimension Icon) was utilized to analyze the thickness of the PG and PG@PyC sheets. X-ray diffraction (XRD, X'Pert PRO, Cu Kα radiation), Raman spectroscopy (Renishaw, inVia Reflex) with a 532 nm laser, and X-ray photoelectron spectroscopy (XPS, ESCALAB Xi +) were employed to characterize the phase compositions. 3D confocal laser microscopy (NANOVEA, ST400) was carried out to measure the average surface roughness of the PG and PG@PyC preforms. X-ray microscope (ZEISS, Xradia 515 Versa, 3D CT) was used to characterize the distribution of PG in the composites.

Measurements of mechanical properties

A universal machine (Edburg, HP-20 and HP-100) was used to evaluate the compressive strength of the PG, pure PyC, and PG@PyC preforms. The dimensions of the samples for compression tests were 10 mm × 10 mm × 10 mm. When the deformation of the preform was 0.0-50.0% (i.e., the thickness of the preform was compressed from 10 mm to 5 mm), stress measurements were recorded. A nanomechanical testing system (Hysitron, TI980) was operated to measure the hardness and elastic modulus of the composites under a load of 5 mN. The tensile strength and compressive strength of the AZ91D and composites were determined by an electromechanical universal testing machine (CMT5504). The tensile test was conducted using specimens with a gauge length of 4.0 mm, a gauge width of 2.0 mm, and a gauge thickness of 1.5 mm. The dimensions of the compressed samples were 4.0 mm in diameter and 6.0 mm in height. The tensile and compressive tests were conducted with a loading speed of 0.5 mm/min at room temperature.

Measurements of electrical conductivity

The electrical conductivity of the preforms was measured using a two-probe method with a digital multimeter (DMM6500). The electrical conductivity of the AZ91D and composites was measured by an eddy current conductivity meter (FIRST, FD101).

Measurements of thermal conductivity

The thermal conductivity of the preforms was evaluated by a thermal constant analyzer (Hot Disk TPS2500S). An infrared camera (InfraTec, VarioCAM hr 384) was used to record the temperature changes of the preforms placed on a heating stage (180 °C).

Measurements of EMI SE values

Vector network analyzer (Anritsu, MS4644A) was applied to test *S*-parameters (S_{11}, S_{12}, S_{21}, and S_{22}) of the PG preform, PG@PyC preforms, and composites from 8.2 to 12.4 GHz (X band). The sample was machined to 22.86 mm × 10.16 mm × 3.00 mm.

Statistics and Reproducibility

The microscope experiments for the preforms and composites (including AFM, SEM, OM, and TEM) were repeated three times independently with similar results. The representative findings are

presented in this paper. For data that includes error bars, the experimental tests were also independently repeated three times. The data are presented as mean values ± standard deviations (SD).

Reporting summary

Further information on research design is available in the Nature Portfolio Reporting Summary linked to this article.

Data availability

The authors declare that data supporting the findings of this study are available within the paper and its Supplementary Information Files. Additional data related to this paper may be requested form the authors. Source data are provided with this paper.

References

1. Ghaffarkhah, A. et al. Ultra-flyweight cryogels of MXene/graphene oxide for electromagnetic interference shielding. *Adv. Funct. Mater.* **33**, 2304748 (2023).
2. Zhang, Q. et al. Millefeuille-inspired biomass alternate multilayer composite, for excellent absorption-dominated, broadband EMI shielding and joule heating. *Compos. Part B* **283**, 111620 (2024).
3. Hao, R. X. et al. Janus structure design of polyimide composite foam for absorption-dominated EMI shielding and thermal insulation. *J. Mater. Sci. Technol.* **206**, 317–326 (2024).
4. Ma, X. F. et al. MOF@wood derived ultrathin carbon composite film for electromagnetic interference shielding with effective absorption and electrothermal management. *Adv. Funct. Mater.* **34**, 2310126 (2023).
5. Park, B. et al. Absorption-dominant electromagnetic interference (EMI) shielding across multiple mmwave bands using conductive patterned magnetic composite and double-walled carbon nanotube film. *Adv. Funct. Mater.* **34**, 2406197 (2024).
6. Nan, Z. et al. Flexible nanocomposite conductors for electromagnetic interference shielding. *Nano-Micro Lett.* **15**, 210–259 (2023).
7. Ke, Q. Q. & Wang, J. Graphene-based materials for supercapacitor electrodes-a review. *J. Materiomics* **2**, 37–54 (2016).
8. Sun, Y. et al. Flexible solid-liquid bi-continuous electrically and thermally conductive nanocomposite for electromagnetic interference shielding and heat dissipation. *Nat. Commun.* **15**, 7290 (2024).
9. Dai, Y. et al. 3D printing of resilient, lightweight and conductive MXene/reduced graphene oxide architectures for broadband electromagnetic interference shielding. *J. Mater. Chem. A.* **10**, 11375–11385 (2022).
10. Cheng, Z. et al. Recent advances in graphene aerogels as absorption-dominated electromagnetic interference shielding materials. *Carbon* **205**, 112–137 (2023).
11. Liu, M. J. et al. A popcorn-inspired strategy for compounding graphene@$NiFe_2O_4$ flexible films for strong electromagnetic interference shielding and absorption. *Nat. Commun.* **15**, 5486 (2024).
12. Wei, Z. P. et al. Influence of the residual oxygen amount in reduced graphene nanoplatelets on microstructure and mechanical properties of ZK60 matrix composites. *Mater. Sci. Eng. A* **842**, 143094 (2022).
13. Tao, J. X. et al. Influence of graphene oxide (GO) on microstructure and biodegradation of ZK30-xGO composites prepared by selective laser melting. *J. Magnes. Alloy.* **8**, 952–962 (2020).
14. Pillari, L. K., Lessoway, K. & Bichler, L. Carbon nanotube and graphene reinforced magnesium matrix composites: a state-of-the-art review. *J. Magnes. Alloy.* **11**, 1825–1905 (2023).
15. Bai, X. Y. et al. Good strength-plasticity compatibility of GNP/AZ31 composites fabricated by FSP: Microstructural evolution and mechanical properties. *J. Mater. Res. Technol.* **20**, 3995–4007 (2022).
16. Sun, X. Y. et al. Microstructures and properties of graphene-nanoplatelet-reinforced magnesium-matrix composites fabricated by an in situ reaction process. *J. Alloy. Compd.* **835**, 155125 (2020).
17. Wang, M. et al. Achieving high strength and ductility in graphene/magnesium composite via an in-situ reaction wetting process. *Carbon* **139**, 954–963 (2018).
18. Du, X. et al. Ultra-high strengthening efficiency of graphene nanoplatelets reinforced magnesium matrix composites. *Mater. Sci. Eng. A* **711**, 633–642 (2018).
19. Shuai, C. J. et al. Interfacial strengthening by reduced graphene oxide coated with MgO in biodegradable Mg composites. *Mater. Des.* **191**, 108612 (2020).
20. Liu, J. et al. Effect of liquid–solid extrusion on the high-temperature compressive properties of C_{sf}/Mg composites. *Mater. Manuf. Process.* **30**, 1391–1396 (2015).
21. Zhang, H. H. et al. Hybridized graphene for supercapacitors: Beyond the limitation of pure graphene. *Small* **17**, 2007311 (2021).
22. Wen, Y. Y. et al. Topological design of ultrastrong and highly conductive graphene films. *Adv. Mater.* **29**, 1702831 (2017).
23. Ma, Y. et al. Multifunctional 3D pristine graphene with tunable electromagnetic properties via self-assembly strategy. *Chem. Eng. J.* **499**, 156224 (2024).
24. Ma, X. F. et al. Ultrathin wood-derived conductive carbon composite film for electromagnetic shielding and electric heating management. *Adv. Funct. Mater.* **33**, 2213431 (2023).
25. Li, K. et al. Conversion of methane to benzene in CVI by density functional theory study. *Sci. Rep.* **9**, 19496 (2019).
26. Zhang, X. et al. A powder-metallurgy-based strategy toward three-dimensional graphene-like network for reinforcing copper matrix composites. *Nat. Commun.* **11**, 2775 (2020).
27. Sun, J. J. et al. Enhancing both strength and toughness of carbon/carbon composites by heat-treated interface modification. *J. Mater. Sci. Technol.* **35**, 383–393 (2019).
28. Zhang, Y. et al. Multifunctional electromagnetic wave absorbing carbon fiber/$Ti_3C_2T_X$ MXene fabric with ultra-wide absorption band. *Carbon* **230**, 119594 (2024).
29. Wang, T. Y. et al. The effect of microstructural evolution on micromechanical behavior of pyrolytic carbon after heat treatment. *Diam. Relat. Mater.* **103**, 107729 (2020).
30. Zhou, P. & Zhao, F. L. 3D evaluation method of cutting surface topography of carbon/phenolic (C/Ph) composite. *J. Wuhan. Univ. Technol.* **26**, 459–463 (2011).
31. Dong, W. P., Sullivan, P. J. & Stout, K. J. Comprehensive study of parameters for characterising three-dimensional surface topography: III: parameters for characterising amplitude and some functional properties. *Wear* **178**, 29–43 (1994).
32. Ma, Y. et al. Collaborative enhancement of thermal diffusivities and mechanical properties of C_{sf}-Cu/Mg composites via introducing Cu coating with different thicknesses. *J. Magnes. Alloy.* **13**, 229–242 (2025).
33. Zhou, A. et al. Understanding the toughening mechanism of silane coupling agents in the interfacial bonding in steel fiber-reinforced cementitious composites. *ACS Appl. Mater. Interfaces* **12**, 44163 (2020).
34. Kang, W. F. et al. Multifunctional submicron SiC fibers for extreme environments: superior electromagnetic absorption and high-temperature performance. *Adv. Funct. Mater.* **35**, 2415432 (2025).
35. Yousefi, N. et al. Highly aligned graphene/polymer nanocomposites with excellent dielectric properties for high performance electromagnetic interference shielding. *Adv. Mater.* **26**, 5480–5487 (2014).
36. Sheng, A. et al. Multilayer WPU conductive composites with controllable electro-magnetic gradient for absorption-dominated electromagnetic interference shielding. *Compos. Part A* **129**, 105692 (2020).

37. Aghajanian, M. K. et al. The fabrication of metal matrix composites by a pressureless infiltration technique. *J. Mater. Sci.* **26**, 447–454 (1991).
38. Qi, L. H. et al. Dynamic measurement on infiltration process and formation mechanism of infiltration front. *T. Nonferr. Metal. Soc.* **20**, 980–986 (2010).
39. Fard, R. R. & Akhlaghi, F. Effect of extrusion temperature on the microstructure and porosity of A356-SiC_p composites. *J. Mater. Process. Tech.* **187-188**, 433–436 (2007).
40. Tekmen, C. et al. The mechanical response of Al-Si-Mg/SiC_p composite: influence of porosity. *Mater. Sci. Eng. A* **360**, 365–371 (2003).
41. Szalva, P. & Orbulov, I. N. The effect of vacuum on the mechanical properties of die cast aluminum AlSi9Cu3(Fe) alloy. *Int. J. Metalcast.* **13**, 853–864 (2019).
42. Cao, H. X. et al. The influence of different vacuum degree on the porosity and mechanical properties of aluminum die casting. *Vacuum* **146**, 278–281 (2017).
43. Alomairy, S. Dissolution mechanism and kinetics of β($Mg_{17}Al_{12}$) phases in AZ91 magnesium alloy. *J. Magnes. Alloy.* **12**, 1581–1592 (2024).
44. Du, Y. et al. Reassessment of the Al-Mn system and a thermodynamic description of the Al-Mg-Mn system. *Int. J. Mater. Res.* **98**, 855–871 (2007).
45. Zeng, G., Xian, J. W. & Gourlay, C. M. Nucleation and growth crystallography of Al_8Mn_5 on B_2-Al (Mn, Fe) in AZ91 magnesium alloys. *Acta Mater.* **153**, 364–376 (2018).
46. Chen, B. L. et al. Influence of microstructures on mechanical properties of the C_{sf}/Mg composite fabricated by liquid-solid extrusion following vacuum pressure infiltration. *J. Alloy. Compd.* **935**, 168083 (2023).
47. Wang, Y. et al. The effect of Al_8Mn_5 intermetallic particles on grain size of as-cast Mg–Al–Zn AZ91D alloy. *Intermetallics* **18**, 1683–1689 (2010).
48. Chen, L. W. et al. Development of AZ91D magnesium alloy-graphene nanoplatelets composites using thixomolding process. *J. Alloy. Compd.* **778**, 359–374 (2019).
49. Viala, J. C. et al. Effect of magnesium on the composition, microstructure and mechanical properties of carbon fibres. *J. Mater. Sci.* **26**, 4977–4984 (1991).
50. Karen, P. et al. The crystal structure of magnesium dicarbide. *J. Alloy. Compd.* **282**, 72–75 (1999).
51. Wang, L. Y. & Chen, T. J. Simultaneously enhancing strength and toughness of graphene oxide reinforced ZK60 magnesium matrix composites through powder thixoforming. *Compos. Part A* **161**, 107097 (2022).
52. Liu, P. S. et al. EMI shielding and thermal conductivity of a high porosity reticular titanium foam. *Mater. Des.* **92**, 823–828 (2016).
53. Chen, M. Y. et al. Carbon nanofiber/polyaniline composite aerogel with excellent electromagnetic interference shielding, low thermal conductivity, and extremely low heat release. *Nano-Micro Lett.* **17**, 80 (2024).
54. Wang, J. H. et al. X-band shielding properties of Mg-9Li matrix composite containing $Ni_{0.4}Zn_{0.4}Co_{0.2}Fe_2O_4$ fabricated by multilayer composite rolling. *J. Alloy. Compd.* **843**, 156053 (2020).
55. Liu, Z. F. et al. Reflection and absorption contributions to the electromagnetic interference shielding of single-walled carbon nanotube/polyurethane composites. *Carbon* **45**, 821–827 (2007).
56. Acharya, S. & Datar, S. Wideband (8-18 GHz) microwave absorption dominated electromagnetic interference (EMI) shielding composite using copper aluminum ferrite and reduced graphene oxide in polymer matrix. *J. Appl. Phys.* **128**, 104902 (2020).
57. Wang, J. H. Simultaneous achievement of high electromagnetic shielding effectiveness (X-band) and strength in Mg-Li-Zn-Gd/MWCNTs composite. *J. Alloy. Compd.* **882**, 160524 (2021).
58. Sun, Z. M. et al. Simultaneously enhanced mechanical properties and electromagnetic interference shielding performance of a graphene nanosheets (GNSs) reinforced magnesium matrix composite by GNSs induced laminated structure. *J. Alloy. Compd.* **898**, 162847 (2022).
59. Xu, Z. Y. et al. GO/MgO/Mg interface mediated strengthening and electromagnetic interference shielding in AZ31 composite. *J. Magnes. Alloy.* **11**, 3800–3814 (2023).
60. Sun, Z. M. et al. Synergistic strengthening of mechanical properties and electromagnetic interference shielding performance of carbon nanotubes (CNTs) reinforced magnesium matrix composites by CNTs induced laminated structure. *Materials* **15**, 300 (2021).
61. Kong, L. et al. Powerful absorbing and lightweight electromagnetic shielding CNTs/RGO composite. *Carbon* **145**, 61–66 (2019).
62. Han, L. Y. et al. Carbon microtube/NiCo carbonate hydride nanoneedle composite foams for broadband electromagnetic interference shielding. *ACS Appl. Nano Mater.* **5**, 4082–4090 (2022).
63. Pandey, R., Tekumalla, S. & Gupta, M. Enhanced (X-band) microwave shielding properties of pure magnesium by addition of diamagnetic titanium micro-particulates. *J. Alloy. Compd.* **770**, 473–482 (2019).
64. Shi, H. L. et al. Achieving significant grain refinement efficiency in Mg-Al alloys via a GNP@MgO composite refiner. *Compos. Part B* **287**, 111822 (2024).
65. Li, Z. et al. A nanodispersion-in-nanograins strategy for ultra-strong, ductile and stable metal nanocomposites. *Nat. Commun.* **13**, 5581 (2022).

Acknowledgements

This work was supported by the National Natural Science Foundation of China (Nos. 52231004, L.H. Qi; 52471164, L.H. Qi; and 52432002, L.J. Guo) and the Innovation Foundation for Doctor Dissertation of Northwestern Polytechnical University (No. CX2024007, Y. Ma). The authors also thank the Analytical & Testing Center of Northwestern Polytechnical University for the characterization of our samples.

Author contributions

Y.M. Conceptualization, investigation, methodology, software, data curation, formal analysis, funding acquisition, and writing - original draft. L.G. Validation, funding acquisition, conceptualization, and methodology. Y.C. Methodology, supervision, visualization, and formal analysis. L.Q. Conceptualization, methodology, writing— review & editing, validation, supervision, and funding acquisition.

Competing interests

The authors declare no competing interests.

Additional information

Supplementary information The online version contains supplementary material available at https://doi.org/10.1038/s41467-025-68266-3.

Correspondence and requests for materials should be addressed to Lehua Qi.

Peer review information *Nature Communications* thanks Zi Ping Wu, and the other, anonymous, reviewer(s) for their contribution to the peer review of this work. A peer review file is available.

Reprints and permissions information is available at http://www.nature.com/reprints

Publisher's note Springer Nature remains neutral with regard to jurisdictional claims in published maps and institutional affiliations.

Open Access This article is licensed under a Creative Commons Attribution-NonCommercial-NoDerivatives 4.0 International License, which permits any non-commercial use, sharing, distribution and reproduction in any medium or format, as long as you give appropriate credit to the original author(s) and the source, provide a link to the Creative Commons licence, and indicate if you modified the licensed material. You do not have permission under this licence to share adapted material derived from this article or parts of it. The images or other third party material in this article are included in the article's Creative Commons licence, unless indicated otherwise in a credit line to the material. If material is not included in the article's Creative Commons licence and your intended use is not permitted by statutory regulation or exceeds the permitted use, you will need to obtain permission directly from the copyright holder. To view a copy of this licence, visit http://creativecommons.org/licenses/by-nc-nd/4.0/.

© The Author(s) 2026